

Embedding parametric resonance in a 2:1 wave energy converter to get a broader bandwidth

*Original*

Embedding parametric resonance in a 2:1 wave energy converter to get a broader bandwidth / Giorgi, Giuseppe. - In: RENEWABLE ENERGY. - ISSN 0960-1481. - (2024). [10.1016/j.renene.2023.119928]

*Availability:*

This version is available at: 11583/2984841 since: 2024-01-04T17:40:13Z

*Publisher:*

Elsevier

*Published*

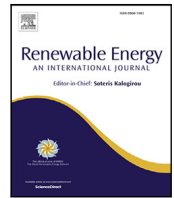
DOI:10.1016/j.renene.2023.119928

*Terms of use:*

This article is made available under terms and conditions as specified in the corresponding bibliographic description in the repository

*Publisher copyright*

(Article begins on next page)



# Embedding parametric resonance in a 2:1 wave energy converter to get a broader bandwidth

Giuseppe Giorgi

Marine Offshore Renewable Energy Lab (MOREnergy Lab), Department of Mechanical and Aerospace Engineering (DIMEAS), Politecnico di Torino, Corso Duca degli Abruzzi 24, Turin, 10129, Italy

## ARTICLE INFO

### Keywords:

2:1 parametric resonance  
Parametric instability  
Wave energy converter  
Nonlinear Froude–Krylov force

## ABSTRACT

The effort to increase the converted power is a common challenge to players in the field of wave energy conversion, both academic and industrial. In the case devices are found to be prone to parametric resonance, it typically has a negative impact on power harvesting and may jeopardize the reliability of the device. This paper makes the case that parametric resonance is not a danger that should be avoided, but rather a chance to achieve a broader system response bandwidth and ultimately increase the amount of power available at the power take-off. Since a time-varying wetted surface causes the highly nonlinear phenomenon of parametric resonance, linear models are unable to fully capture this instability. As a result, nonlinear Froude–Krylov forces are herein implemented via a computationally effective method for prismatic floaters that is compatible with both exhaustive simulation methods and real-time computing, as the whole simulations runs up to 50 times faster than real-time. A novel pendulum-based device is intentionally defined to exhibit a 2:1 ratio between heave and pitch natural frequencies, causing parametric instability. Results demonstrate that linear models predict a single zone of meaningful potential power extraction around the pitch natural frequency, as expected; however, by using the designed attitude to develop parametric instability, a second additional region develops near the heave natural period. As a result, the free response bandwidth is in fact increased, making more energy available at the power take-off axis thanks to the nonlinear instability embedded in the wave energy converter.

## 1. Introduction

Despite significant technological advances in recent years, the wave energy sector still faces the major challenge of reducing the levelised cost of electricity (LCoE) to become competitive with other forms of renewable energy and attractive to public and private investors [1]. On the one hand, efforts are being made to reduce capital and operational costs: techno-economic optimizations [2] are based on cost functions that, although difficult to estimate due to a still immature industry [3], are becoming more representative and informative of the real system thanks to bottom-up approaches [4]. On the other hand, the complementary path to LCoE reduction is to increase the overall productivity [5], expanding the frequency bandwidth of the device to make it perform well under a wide range of wave conditions [6], thus achieving a higher capacity factor [7]. The main tool to increase the power efficiency, especially far from the natural frequency of the system, is optimal control: normally using the Power-Take-Off (PTO) system, the control strategy applies an action aimed at changing the free response of the device (the *baseline*) to achieve the control objective, which typically includes the converted energy. Under ideal

conditions, where the PTO action can be arbitrarily chosen, the optimal control action can change the system dynamics to virtually any extent to optimize performance. However, practical physical constraints (typically on force, displacement, and/or velocity) limit the range of action of the control such that the controlled response lies within the neighbourhood of free response, as close as tight the constraints are; it follows that realistic optimal control with tight constraints results in a much lower improvement over the baseline. Therefore, although it is tempting to rely on optimal control alone to enhance productivity, it is still necessary to increase the free response: to this purpose, also design should be optimized (ideally in conjunction with control) to provide a fruitful baseline that a realistic (constrained) control can practically lead to optimal power generation. Such significant design changes, ranging from operating principles and subsystem configurations to geometry and dimensions, should be performed at low Technology Readiness Levels (TRLs), when costs are relatively low and failures are not catastrophic [8]. However, knowledge of the system may still be superficial at low TRLs, because experience is limited and numerical models may not be reliable. The effectiveness of holistic techno-economic optimizations in a real-world application depends on

E-mail address: [giuseppe.giorgi@polito.it](mailto:giuseppe.giorgi@polito.it).

<https://doi.org/10.1016/j.renene.2023.119928>

Received 17 July 2023; Received in revised form 13 December 2023; Accepted 29 December 2023

Available online 31 December 2023

0960-1481/© 2023 The Author(s). Published by Elsevier Ltd. This is an open access article under the CC BY license (<http://creativecommons.org/licenses/by/4.0/>).

the representativeness of their underlying numerical models. Nevertheless, due to the stringent requirement of low computational time, design definition and optimizations are performed using either linear [9], linearized [10], spectral [11], or reduced models [12]. Within this context, accuracy is usually interpreted as a gradient, with gradually higher accuracy for incrementally more complex models [13]. Based on the hypothesis that accuracy is a gradient, the real behaviour of the wave energy converter (WEC) is assumed to lie within a certain error range that is roughly proportional to the complexity of the model. However, the accuracy of the representation of certain nonlinear phenomena is Boolean (yes or no) rather than a gradient, in the sense that they are either articulated or completely overlooked [14]. This is the case of *parametric resonance*, which is a type of instability that can only be captured by models that account for time-varying wetted surfaces; therefore, linear models are completely blind to parametric resonance. When present, it is usually discovered well after design, likely in the first experimental tests [15]; it usually is detrimental and late mitigation actions are sought [16].

In this paper, it is argued that, if properly embedded early in the design phases, parametric resonance can actually be exploited to improve power conversion capabilities. The strategy of leveraging strongly nonlinear phenomena is common, if not fundamental, in mechanical vibration energy harvesters (VEHs) [17]; conversely, only seldom examples can be found in wave energy applications. The reason why this is quite uncommon in the wave energy field is that numerical models typically able to articulate parametric resonance are time-consuming and not suitable for early design applications, while nonlinear solid mechanical systems are relatively easy to be modelled. In this paper, a computationally efficient mathematical formulation is briefly presented and used, based on a recent description of nonlinear Froude-Krylov forces for prismatic floaters [18], which is computationally compatible with early design applications and extensive simulations, as well as an input generator for data-driven system identification approaches. Based on this mathematical model, a 2:1 parametric resonance condition is prescribed for the conceptual definition of a novel inertial WEC with a broader bandwidth than its linear counterpart.

The remainder of the paper is organized as follows: Section 2 describes parametric resonance, when it is detrimental (most cases) and a few examples when it is exploited (within and outside wave energy field). Section 3 proposes a WEC that is purposely designed to be prone to parametric resonance, with the objective to have a broader free response bandwidth. Section 4 presents the computationally efficient numerical model that can articulate such a nonlinear phenomenon. Finally, Section 5 presents results and Section 6 provides some discussion to get further insights, while Section 7 draws final conclusions.

## 2. Parametric resonance in energy harvesters

Time-variations of one or more parameters of a system may induce it into parametric resonance, which is a mechanism for internal excitation [19]. The standard approach in nonlinear dynamics to preliminarily describe such a phenomenon is via a Mathieu-type of instability [20]: it is a single degree of freedom (DoF) second-order differential equation of motion of the generic variable  $\chi$ , where the stiffness term varies with time ( $t$ ) following a harmonic function with circular frequency ( $\omega_c$ ); in real engineering applications, the damped Mathieu equation is considered:

$$\ddot{\chi} + \mu \dot{\chi} + (\Delta + \Lambda \cos \tau) \chi = 0, \quad (1)$$

where the time-derivatives are with respect to the dimensionless  $\tau = \omega_c t$ ,  $\Delta$  represents a dimensionless stiffness,  $\Lambda$  is the dimensionless amplitude of the stiffness variation, and  $\mu$  is the dimensionless damping coefficient. The consequent stability diagram of Eq. (1) is shown in Fig. 1, where  $\omega_n$  is the natural frequency of the 1-DoF system and  $\Delta^2 = \omega_n / \omega_c$ ; two conditions for instability (shaded areas in Fig. 1) arise:

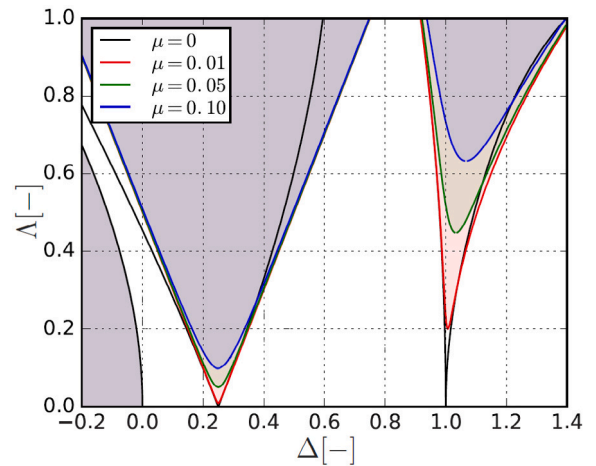


Fig. 1. Stability diagram of the damped Mathieu equations ( $\mu$  is the damping), shown in (1). Unstable regions are shaded; they arise when the excitation frequency is twice ( $\Delta = 0.25$ ) or equal ( $\Delta = 1$ ) to the natural frequency of the system, and for sufficiently large excitation amplitude (increasing  $\Lambda$ ).

1. The excitation frequency ( $\omega_c$ ) is twice of or equal to the natural frequency ( $\omega_n$ ) of the system ( $\Delta = 0.25$  or 1, respectively)
2. The excitation amplitude exceeds internal dissipations of the system (increasing  $\Lambda$ )

Despite the fact that the Mathieu equation can only provide some insights on the conditions triggering parametric resonance, and not on the quantitative estimation of its severity [15], it can still guide interpretation of experimental behaviour and potentially inspire convenient design choices (as in this paper). Hereafter, Section 2.1 briefly discusses how parametric resonance is often just a detrimental phenomenon for wave energy conversion; conversely, Section 2.2 presents virtuous examples where it is leveraged as an enabling factor to make energy conversion viable, most commonly in vibration energy harvesters and rarely in the wave energy field.

### 2.1. Parametric resonance as a detrimental phenomenon

Parametric resonance is a well-known phenomenon in traditional marine engineering, currently being extensively examined because of the serious safety and cost issues it raises [20]. Numerous techniques to detect and avoid parametric roll are being developed and implemented. Large cargo ships are particularly concerned in this issue because undetected parametric roll instability can result in cargo loss and even crew injury [21]. Similarly, spar-like structures can experience significant rotations due to parametric resonance [22]; since such structures (typically for oil extraction or floating offshore wind turbines) are expected to have small rotations to be fit for purpose, parametric resonance is not desirable. Additionally, the station-keeping system should be designed with sufficient knowledge of the types of motions that will occur during operation.

In the wave energy field, parametric resonance has been observed in some floating systems consisting of either a tethered body or a self-referenced two-body system: in an offshore oscillating water column [23], in a floating sloped device [24], in pendulum-based [25] or two-body [26] self-referenced WECs, and in a bottom-tethered system [27]. In each of these scenarios, parametric resonance decreases the efficiency of energy conversion by rerouting a portion of the energy away from the degree of freedom where the PTO is installed, and thereby decreasing the amount of energy that is available. Additionally, higher and perhaps unexpected loads may be transferred to other WEC subsystems, particularly the mooring system, raising the possibility of damage and decreasing dependability. To prevent an increase in parametric instability, dedicated detection and suppression strategies are put in place to avoid the rise of parametric instability [28].

## 2.2. Parametric resonance as an enabling phenomenon

When properly incorporated into early design phases, parametric resonance can be a way to obtain a broader bandwidth and increase power yields. In fields other than wave energy, particularly in the field of mechanical vibration energy harvesting, nonlinearities and instabilities are frequently considered to be a system's primary strength rather than its weakness. Indeed, the frequency response curve of linear VEHs is typically sharp and narrow, rendering energy generation unprofitable; therefore, nonlinearities are typically introduced into the system to increase their bandwidth [17]: parametrically excited non-linear energy harvester [29], 1:2 internal resonance embedded condition in cantilever VEHs [30], parametric oscillators [31], bistability [32], among others. The simplicity of the underlying nonlinear mathematical model, which is typically algebraic and completely white (i.e., transparently based on physical quantities), is primarily the reason instability-based working principles are so popular in VEH.

There are a few examples of WECs that use parametric resonance to improve energy extraction. Most concepts are based on inertial coupling between a float and one [33] or more [34] pendula; in some concepts, rotational control may be required to initiate and maintain parametric rotation [35], possibly realized via length adjustments [36]. In [37], a single float system is considered, where a control strategy can account for the nonlinear hydrodynamic coupling between buoyancy and surge/pitch, such that the energy extracted from buoyancy is increased. [38] considers a WEC with two concentric floats where the parametric resonance is induced by modulating the mass. A negative stiffness mechanism is used for a raft-type device in [39], while [40] implements a bistable mechanism in a wave energy converter. Other methods to increase power extraction comprise increase the number of active degrees of freedom and leverage linear and nonlinear coupling between them, as in [41] for an inertial device, and in [42] for a point absorber.

## 3. A 2:1 parametric resonance pitching WEC

This study focuses on WECs that derive power from the pitching motion of a floater, either directly (for example, through the use of a fixed reference structure) or indirectly (for example, through the use of inertial coupling with an internal mechanism); numerical results are produced for a case study involving inertial coupling, though the notional considerations are more general.

Evidences from [37] or [18] have shown that heave and pitch DoFs are linearly independent but hydrodynamically coupled once the instantaneous wetted surface is taken into account in the calculation of the excitation forces, especially in the case of the nonlinear Froude–Krylov component. Therefore, it is argued in this work that a WEC specifically designed for a 2:1 ratio between the natural frequency of heave and pitch would greatly benefit from the resulting parametric resonance. Under conditions of parametric instability (Section 3), some of the incoming energy would be redirected from the heave DoF to the pitch DoF, making it available for conversion by the PTO.

To test such an assumption and to obtain initial quantitative results on the significance of the benefits, if any, a case study is herein formulated. The Pendulum Wave Energy Converter (PeWEC) is considered as a baseline [43], which is a sealed float containing a pendulum: when the hull pitches in response to incoming waves, oscillations of the pendulum are induced by the inertial coupling, and damped by the PTO. A schematic representation of a PeWEC-like device is shown in Fig. 2. The geometry, dimensions, and mass properties of the PeWEC-like device are inspired by [18,44]; however, the pitching inertia of the system is artificially modified so that the heaving natural period ( $T_3$ ) is half of the pitching natural period ( $T_5$ ), i.e., a 2:1 ratio between the respective natural frequencies.

It should be noted that the present case study has the objective of a proof of concept, while evaluating the actual performance [45] of real

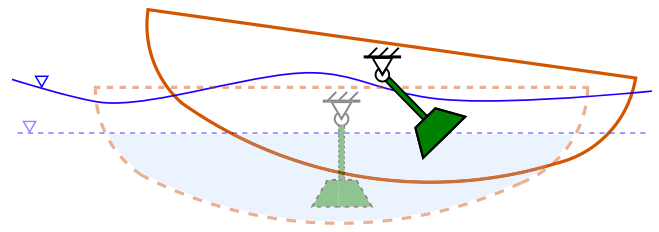


Fig. 2. A pendulum in a sealed hull is shown in the schematic diagram of a wave energy converter inspired by the PeWEC. While the solid lines depict a displacement in sea water, the transparent body is shown in a resting state in still water.

wave energy converters is a complex task; the final productivity and effectiveness of design improvement is highly dependent on detailed wave resource characterization [46], eventually including appropriate bias correction [47]. In fact, the representative yearly occurrence of panchromatic waves should be considered for a thorough evaluation of the annual energy production; however, the purpose of this work is to provide a first go/no-go decision to assess the potential of the concept herein proposed.

## 4. Mathematical modelling

Studying the effects of parametric resonance caused by the nonlinear coupling between the degrees of freedom of heave and pitch is the goal of this work. In order to enable meaningful and unambiguous observations, the mathematical model and setup are carefully chosen; in particular, confounding factors are eliminated to ensure a clear, transparent, and unambiguous inference of causality. As a result, the following simulation conditions are set:

- *Monochromatic waves*: Since parametric resonance is a frequency-dependent phenomenon, regular waves are considered to clearly discriminate trends in the dynamic response of the system. In addition, to study potential hysteresis and bifurcation phenomena, up-chirp and down-chirp signals are also considered [19].
- *Time-domain model*: described in Section 4.1, it is necessary to numerically solve nonlinear systems in the time domain.
- *Nonlinear Froude–Krylov (NLFK) force*: it is the only nonlinearity included in the system, described in Section 4.2, since it can articulate parametric resonance; all other nonlinear effects are neglected (i.e., viscosity, PTO saturations, pendulum kinematics, moorings, etc.), so that any nonlinear behaviour is univocally due to NLFK.
- *Only heave and pitch hydrodynamic DoFs*: being linearly uncoupled, any coupling in the nonlinear response only depends on the parametric resonance, which activates an internal energy exchange between such DoFs. It should be noted that the surge simulation would have been a confounding factor because it would have introduced a linear coupling with pitch and therefore an additional direction of energy flow; moreover, it would have required an additional term for station-keeping in the equation of motion.
- *No PTO*: Considering the free response of the device is paramount to articulate its inherent characteristics and evaluate the raw energy availability; this can then be leveraged by an appropriate control system, acting through the PTO force.

### 4.1. Time domain model

The only distinction between the two time domain models herein implemented is whether linear (LFK) or nonlinear (NLFK) static and dynamic Froude–Krylov forces are included. Regular waves are taken into consideration, and their heights and periods are selected using a typical bivariate distribution [48].

Let us consider first the linear equation of motion of the 2 hydrodynamic DoFs only, i.e. heave and pitch, defined about the centre of gravity and in the frequency domain as follows:

$$[-\omega^2 (\mathbf{M} + \mathbf{A}(\omega)) + j\omega\mathbf{B}(\omega) + \mathbf{K}_h] \xi_2 = \mathbf{F}_d + \mathbf{F}_{FK_d} \quad (2)$$

where  $\xi_2$  is the  $2 \times 1$  state vector, composed of heave ( $z$ ) and pitch ( $\theta$ ),  $\mathbf{M}$  the diagonal inertia matrix,  $\mathbf{A}(\omega)$  and  $\mathbf{B}(\omega)$  the diagonal frequency-dependent added mass and radiation damping,  $\mathbf{K}_h$  the diagonal linear hydrostatic stiffness,  $\mathbf{F}_d$  and  $\mathbf{F}_{FK_d}$  are the diffraction and linear dynamic FK forces, whose sum gives the total hydrodynamic excitation force  $\mathbf{F}_{ex}$ .

The linear hydrodynamic curves are computed for the mean wetted surface of the floater via a linear Boundary Element Method (BEM) software, such as Nemoh [49] or WAMIT [50]. The NLFK version of (2) alternatively computes  $(\mathbf{F}_{FK_d} - \mathbf{K}_h \xi_2)$  in a nonlinear way, as described in Section 4.2.

The resulting linear hydrodynamic curves are presented in Appendix A. Diffraction, dynamic Froude–Krylov, and their sum (excitation), are presented in Fig. 9: dynamic FK components are significantly larger in magnitude than diffraction, making the NLFK approach representative of nonlinear hydrodynamic interactions due to the time-varying wetted surface. The phase shift of the linear hydrodynamic forces with respect to the incoming wave is constant for FK, and almost-constant for diffraction within the range of physically meaningful wave frequencies; however, the nonlinear representation of NLFK forces may show a drift of the phase difference with increasing wave amplitude [51]. Finally, note that heaving and pitching driving forces have a phase shift of about 90 degrees.

Radiation force coefficients, depending on the incoming wave frequency, are presented in Fig. 10. The total radiation force in the frequency domain is given by:

$$\mathbf{F}_{rad}(j\omega) = [\omega^2 \mathbf{A}(\omega) - j\omega\mathbf{B}(\omega)] \xi_2(j\omega) \quad (3)$$

It is possible to translate (3) from frequency to time domain as follows [52]:

$$\mathbf{F}_{rad}(t) = -\mathbf{A}_\infty \ddot{\xi}_2 - \int_0^t \mathbf{K}(t-t') \dot{\xi}_2(t') dt' = -\mathbf{A}_\infty \ddot{\xi}_2 - \mathbf{F}_{con}(t) \quad (4)$$

where the time and frequency dependence are loosely used for simplicity, and the kernel of the convolution integral ( $\mathbf{K}$ ) is the impulse response function, also known as retardation function. The added mass at infinity ( $\mathbf{A}_\infty$ ) and  $\mathbf{K}$  can be computed from the  $A$  and  $B$  as follows:

$$\mathbf{A}_\infty = \lim_{\omega \rightarrow \infty} \mathbf{A}(\omega) \quad (5a)$$

$$\mathbf{K}(t) = \frac{2}{\pi} \int_0^\infty \mathbf{B}(\omega) \cos(\omega t) d\omega \quad (5b)$$

From the computational point of view, (4) is typically considered prohibitive, due to the integration to infinity of the memory effect provided by the convolution term. Therefore, it is common practice to apply system identification techniques to obtain a state space representation of  $\mathbf{F}_{con}(t)$  for a generic DoF  $\chi$ :

$$\begin{cases} \dot{\boldsymbol{\kappa}} = \mathbf{A}^{ss} \boldsymbol{\kappa} + \mathbf{B}^{ss} \chi \\ \mathbf{F}_{con}(t) = \mathbf{C}^{ss} \boldsymbol{\kappa} \end{cases} \quad (6)$$

Since heave and pitch DoFs are hydrodynamically uncoupled, the state space representation of (6) can be performed separately for each DoF, leading to the following triplets for heave ( $\mathbf{A}_z^{ss}$ ,  $\mathbf{B}_z^{ss}$ ,  $\mathbf{C}_z^{ss}$ ) and pitch ( $\mathbf{A}_\theta^{ss}$ ,  $\mathbf{B}_\theta^{ss}$ ,  $\mathbf{C}_\theta^{ss}$ ). Such parameters, identified with a moment-matching approach [53], are presented in Appendix A.

Finally, the mechanical coupling between the external hull, subject to the incoming waves, and the internal pendulum, is considered. A Jacobian linearization of the Lagrangian equation of motion is implemented, which has been extensively validated in wave tank tests for the PeWEC device [54]. The resulting complete time domain model is presented in Appendix B,

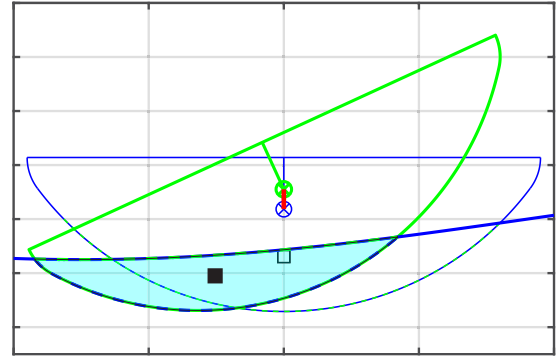


Fig. 3. Snapshot of a displaced hull, depicted as a green thick solid line, with the blue thick solid line representing the instantaneous free surface elevation and the shaded area representing the instantaneous submerged volume. The position of the centre of gravity is indicated by the crossed circle, and the centre of buoyancy is indicated by the square (empty: LFK; full: NLFK). The rest position (LFK) is shown in thin line. Source: Adapted from [18].

#### 4.2. Nonlinear Froude–Krylov force model

Since parametric resonance is due to time-varying parameters of the system, nonlinear Froude–Krylov forces are well suited numerical tools; in fact, NLFK forces are calculated as the integral of the pressure of the unperturbed wave field onto the instantaneous wetted surface ( $S_w(t)$ ). Engineering studies relying on simulating results in real-time and/or numerous iterations in a short period of time require models with a reasonable computational cost. Axisymmetric and prismatic floaters can benefit from a computationally effective analytical description of NLFK integrals, whereas geometries of arbitrary complexity may necessitate mesh-based NLFK methods that are frequently very computationally intensive. The device herein considered is prismatic, meaning that its geometry is invariant in the horizontal direction that is perpendicular to the wave propagation and parallel to the wave front.

Although throughout details of the NLFK integration method for prismatic floaters are given in [18], a brief summary is presented hereafter. Assuming two-dimensional waves in the  $(x, z)$  coordinate system, where  $x$  is the direction of propagation of the wave, and  $z$  is the vertical axis, positive upwards, with the origin at the still water level (SWL),  $a$  the wave amplitude,  $\omega_w$  the wave frequency,  $k$  the wave number,  $h$  the water depth, and  $z'$  the vertical coordinate modified according to Wheeler's stretching [55], the total undisturbed pressure ( $p_u$ ) follows:

$$p_u = -\rho g z + a \cos(\omega_w t - kx) \frac{\cosh(k(z' + h))}{\cosh(kh)}, \quad (7)$$

where  $\rho$  is the water density and  $g$  the acceleration of gravity.

Froude–Krylov generalized forces ( $\mathbf{F}_{FK}$ ), divided into linear forces ( $\mathbf{f}_{FK}$ ) and torques ( $\boldsymbol{\tau}_{FK}$ ), integrate the undisturbed pressure field ( $p_u$ ), shown in (7), as follows:

$$\mathbf{f}_{FK}(t) = \mathbf{f}_g + \iint_{S_w(t)} p_u(x, y, z, t) \mathbf{n} dS, \quad (8a)$$

$$\boldsymbol{\tau}_{FK}(t) = (\mathbf{r}_g - \mathbf{r}_R) \times \mathbf{f}_g + \iint_{S_w(t)} p_u(x, y, z, t) (\mathbf{r} - \mathbf{r}_R) \times \mathbf{n} dS, \quad (8b)$$

where  $\mathbf{f}_g$  is the gravity force,  $\boldsymbol{\tau}_g$  its contribution to the torque,  $\mathbf{n}$  is the unity vector normal to the surface,  $\mathbf{r}$  is the generic position vector,  $\mathbf{r}_R = (x_R, y_R, z_R)'$  is the reference point around which the torque is computed, and likewise  $\mathbf{r}_g$  is the position vector of the centre of gravity.

Generic NLFK solvers for arbitrary complex floaters rely on a meshed discretization of  $S_w(t)$  that becomes the computational bottleneck, that may be incompatible with extensive analysis of nonlinear dynamics behaviour requiring many long iterations. Therefore, in this paper, a faster analytical representation is used, which is available for

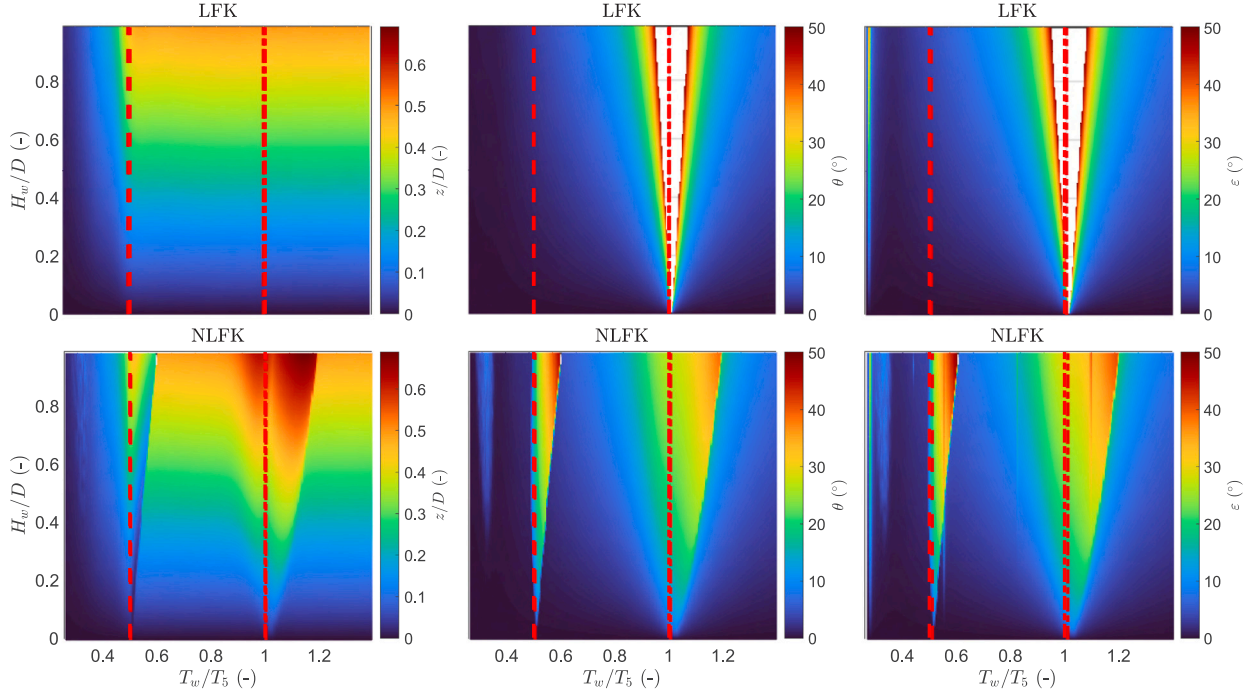


Fig. 4. From left to right: amplitudes in normalized heave ( $z/D$ ), pitch ( $\theta$ ), and the pendulum oscillation ( $\epsilon$ ), plotted with respect to the normalized wave period ( $T_w/T_5$ ) and normalized wave height ( $H_w/D$ ); top and bottom rows refer to LFK and NLFK models, respectively. The dashed and dash-dotted lines highlight  $T_w/T_5$  equal to 0.5 and 1, respectively.

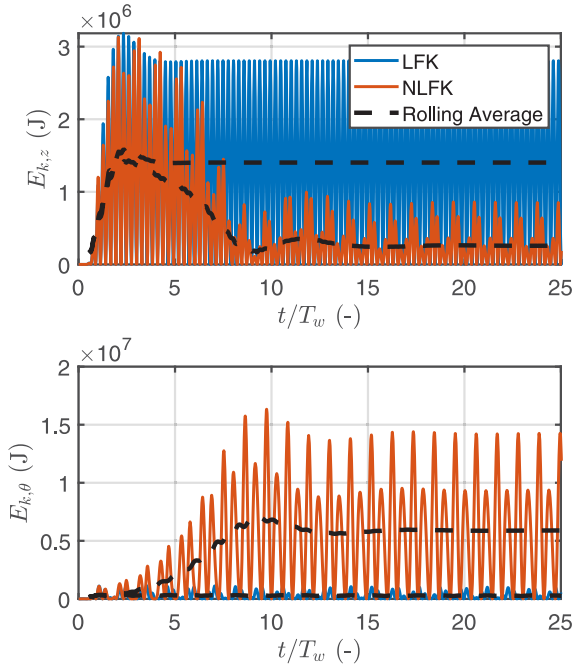


Fig. 5. Instantaneous kinetic energy in heave (top) and pitch (bottom) for a wave with  $T_w = 0.55T_5$  and  $H_w = 4\text{m}$ .

both axisymmetric and prismatic floaters [56]. This method leverages the simplified geometry to obtain an analytical definition of the keel of the hull as it moves, hence enabling the analytical representation of the instantaneous wetted surface, as graphically shown in Fig. 3. Finally, an

explicit definition of integrals in (8) is obtained, which are then solved numerically.

The computational time of the NLFK force method depends on the required relative and absolute accuracy of the numerical integration, as well as on the states of the simulation, the time-step and the time-integration scheme; however, the variability is relatively small. For the simulations performed in this paper, the NLFK model is only about 100 times slower than the LFK model. The relative computational time, defined as the total simulation time divided by the simulated time, or alternatively as the time required to simulate one time step, is between 2% and 3%. This means that NLFK simulations run between 30 and 50 times faster than real time.

## 5. Results

Time-domain simulations are performed for a dense grid of monochromatic waves, sweeping wave periods ( $T_w$ ) and wave heights ( $H_w$ ) to include relevant operational conditions [48]. In addition, with the objective to highlight parametric resonance behaviour,  $T_w$  ranges from 0.25 to 1.4 times the natural period in pitch ( $T_5$ ); likewise,  $H_w$  is defined as a ratio of the draft ( $D$ ) of the floater at rest, ranging from 0 to 1. The initial transient is smoothed by applying sigmoid weighting function from 0 to 1 during the first five wave periods of the incoming free surface elevation. Sufficiently long time-domain simulations are run to ensure reaching a smooth and periodic response at the steady state. At the conclusion of the simulation, the motion amplitude is calculated as the difference between the signal's peak and trough over a time window; the time window's length is  $2T_w$  to take into account the anticipated period doubling brought on by parametric resonance. Fig. 4 presents such amplitudes in normalized heave ( $z/D$ ), pitch ( $\theta$ ), and the pendulum oscillation ( $\epsilon$ ), plotted with respect to the normalized wave period ( $T_w/T_5$ ) and normalized wave height ( $H_w/D$ ), according to LFK and NLFK models. Meaningful ratios of  $T_w/T_5$  are highlighted

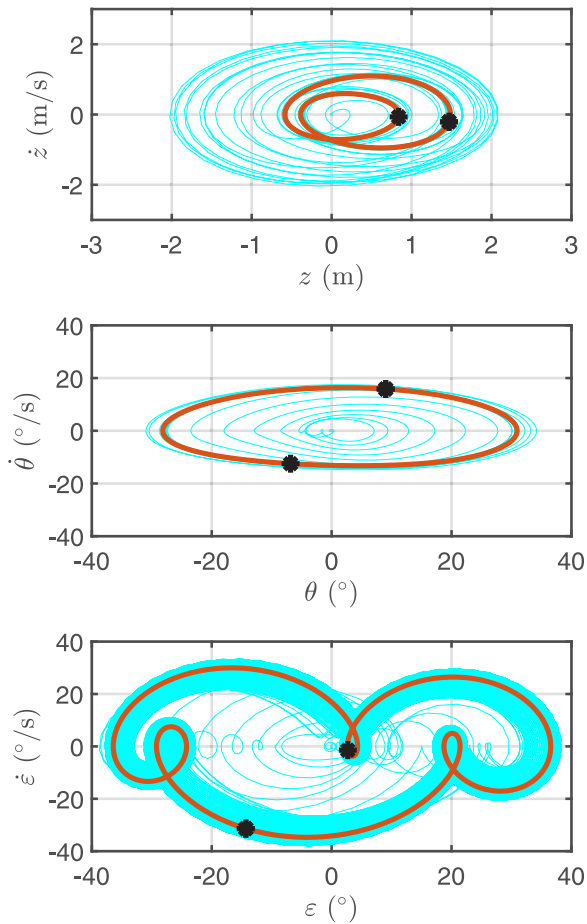


Fig. 6. Stroboscopic phase diagram for a wave with  $T_w = 0.55T_5$  and  $H_w = 4\text{m}$ . The transient is presented in thin cyan line, the steady state in thick orange line, and bold markers are plotted every  $T_w$  during the limit cycle.

with 2 red lines: a dash-dotted line is located at  $T_w = T_5$ , whereas a dashed line highlights  $T_w = T_3 = 0.5T_5$ , following the 2:1 resonance condition imposed in Section 3, i.e. both the heave natural period and the simplified parametric resonance condition.

The linear response (top row of Fig. 4) shows no coupling between pitch and heave, as expected. The peak response in each DoF is reached at their respective natural frequency ( $T_w = T_3 = 0.5T_5$  for heave, and  $T_w = T_5$  for pitch); the inertial coupling makes the pendulum oscillation follow directly the pitching response, as the pendulum natural period is significantly lower (about  $\frac{1}{4}T_5$ ). Following the hypothesis discussed in Section 4, the LFK model is fully linear and not dampened, and no saturation or end-stop is included; the direct consequence is that unrealistic responses are predicted by the LFK model close to the pitching natural frequency. Therefore, to improve readability and enable meaningful discussion, any oscillation above  $50^\circ$  is excluded from Fig. 4 (white area).

The nonlinear response (bottom row of Fig. 4) is presented with the same colour scale of the LFK model, to facilitate qualitative comparison of the resulting amplitudes of motion. It is evident that a nonlinear coupling occurs at both highlighted normalized wave periods. In particular, at  $T_w = 0.5T_5$ , the heave response decreases with respect to the LFK model, with a clear wedge incision in the response scatter; the same wedge is found in the  $\theta$  and  $\epsilon$  responses, highlighting how parametric resonance effectively redirects part of the energy away from the heaving DoF. Notably, the linear model almost completely fails to predict the response at this frequency, indicating that parametric resonance is the only excitation mechanism introduced as a result of the 2:1 ratio prescribed during the design phase (see Section 3).

While the left edge of the wedge remains vertical as  $H_w$  increases, the right edge shifts at higher periods, giving the wedge an asymmetric appearance with respect to the vertical line  $T_w = 0.5T_5$ . As a result, the range of the parametric resonance response expands, and since the wave energy content is proportional to  $T_w$  and to  $H_w^2$  [57], the amplitude of the parametric response increases for larger wave periods. This behaviour is in line with the qualitative prediction of the Mathieu diagram shown in Fig. 1, which states that once the system's internal damping is overcome, the width of the instability region increases for higher input energy.

Similarly, nonlinear coupling also occurs at  $T_w = T_5$ ; however, in this case, the energy flow is reversed because the heave response at  $T_w = T_5$  is higher than in its neighbourhood. Based on the simulation conditions, it is not possible to judge whether this is detrimental or beneficial to energy production, since the LFK response in pitch is unrealistic and cannot provide a meaningful comparison benchmark. Assuming that the total mechanical energy absorbed by the entire system is constant, parametric resonance removes some of the energy from pitch to achieve a higher heaving response and would therefore be detrimental. However, parametric instability may result in an overall higher response, providing more mechanical energy at the floater; in this case, parametric resonance may still have a net positive effect at the PTO axis, in spite of the higher heave response.

It is also worth noting that the pitch and, consequently, the pendulum swing are lower than the LFK prediction and never take unrealistic values. This is specifically due to the use of a representative NLFK model that accounts for the floater's actual instantaneous wetted surface.

Finally, Fig. 4 bring evidences that inducing parametric resonance indeed has had the effect of enlarging the potential bandwidth of available energy conversion, since the PTO axis is excited in a wider range of wave periods, i.e. close to  $0.5T_5$  and  $T_5$ . In addition, the magnitude of the induced oscillation at the nonlinear 2:1 parametric resonance is comparable to the response at the linear natural period; therefore, the enhancement brought by parametric resonance is significant and worth of further investigation.

Such a modification of the free response of the system can be exploited by a control strategy if and only if its underlying numerical model is capable of articulating parametric resonance (if model-based controllers are used). Such a nonlinear controller could act on the system to trigger parametric instability and eventually amplify the severity of the parametric response. However, incorporating complex nonlinearities into a control-oriented numerical model is a challenging task: promising approaches are based on identification data-driven techniques, which have already been proven effective for NLFK-type nonlinearities [58].

Having Fig. 4 proven that the 2:1 parametric resonance condition does bring to a broader bandwidth across different relevant sea state conditions, Section 6 provides further insight on the time domain evolution of the response, especially in the parametric resonance region, investigating the transient, the gradual build-up of instability, and bifurcation behaviour that may be relevant to be taken into account during the design of the system and of the control strategy.

## 6. Discussion

The increase of the amount of available energy at the PTO axis is deduced from the steady-state response to monochromatic waves, presented in Fig. 4; it is also worth to directly analyse the kinetic energy, and evaluate the length of the transient required to build up a sustained parametric response. Fig. 5 plots the instantaneous kinetic energy in heave ( $E_{k,z}$ ) and pitch ( $E_{k,\theta}$ ), for a representative wave in the 2:1 wedge of Fig. 4, i.e. at  $T_w = 0.55T_5$  and  $H_w = 4\text{m}$ . Given the oscillatory nature of the instantaneous kinematic energy, a rolling average is also plotted in dashed line to facilitate the analysis of the transient. Linear and nonlinear models are compared, to highlight the

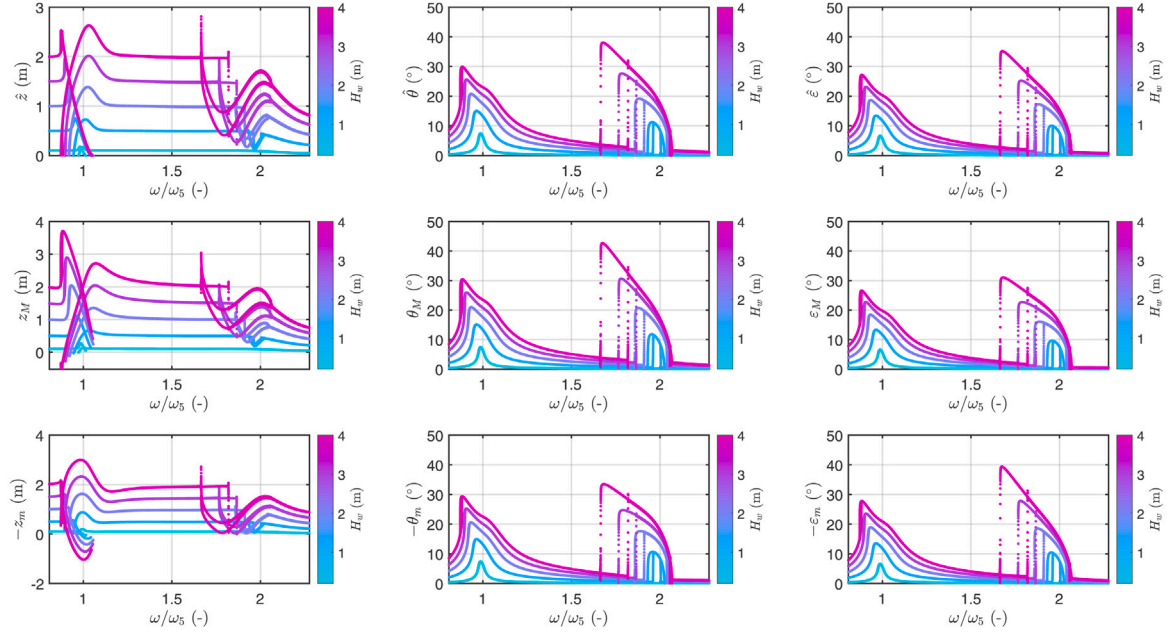


Fig. 7. Amplitudes (top row), maxima (mid row), and minima (bottom row) of the time-trace response to the up/down-chirp signals with linearly increasing/decreasing instantaneous frequency ( $\omega$ ).

differences in available energy and the length of the transient. The time axis is normalized by the wave period, to indicate the number of wave cycles. As long as the pitch response is low, in the first wave cycles, LFK and NLFK are similar. However, as parametric resonance gradually pumps energy from heave to pitch, the instability builds up; after about 15 wave periods, the transient is fully elapsed, as highlighted by the steady-state available energy.

Fig. 5 also shows suggests the nonlinear response has a period doubling. To better visualize the characteristics of the limit cycle, a stroboscopic phase diagram is shown in Fig. 6, for the same wave as in Fig. 5. The transient is presented in thin cyan line, the steady state in thick orange line, and bold markers are plotted every  $T_w$  during the limit cycle. In all DoFs, two distinct markers along the limit cycle confirm the period doubling: the heave response presents two local maxima of the positive displacement, i.e. two alternating amplitudes, while the pitch limit cycle is elliptical, hence with the amplitude of the response spanning over two wave periods. The topology of the pendulum oscillation is richer, with three loops across the  $2T_w$  steady response. It is also worth highlighting that the transient for  $\varepsilon$  is much longer, as shown by the dense bundle of thin cyan lines: in fact, while heave and pitch are subject to radiation damping, the pendulum has only a very small viscous damping  $B_p$  to describe friction effects at the hinge, whereas no PTO is included.

As already discussed, the nonlinear response of the system strongly depends on the excitation frequency. Fig. 4 is obtained with regular waves, namely monochromatic harmonic functions, that gradually bring the system to steady state starting from equilibrium initial conditions at rest with a smoothed excitation force. On the one hand, regular waves are physically plausible, since real waves are a superposition of harmonic functions; on the other hand, monochromatic excitation does not allow to explore potential bifurcation and hysteresis behaviour. In addition, a comprehensive analysis of the  $T_w$  space may be computationally demanding, since a refined period spacing should be explored and simulations should be long enough to reach steady state. Therefore, it is convenient to also consider a physically-unrealistic but informative chirp signal, that can provide useful insight on the nonlinear behaviour of the system, in a computationally compact way.

In this paper, a fictitious chirp free surface elevation ( $\eta$ ) is considered, with frequency linearly changing with time, defined as:

$$\begin{cases} \eta = \frac{H_w}{2} \cos\left(\left(\frac{\xi}{2}t + \omega_0\right)t\right) \\ c = \frac{\omega_1 - \omega_0}{T} \end{cases} \quad (9)$$

where the frequency sweep goes from  $\omega_0$  to  $\omega_1$  within a time window  $T$ , and the resulting instantaneous frequency is given as  $\omega = ct + \omega_0$ . Both up-chirp and down-chirp are investigated, referring to the relative comparison of  $\omega_0$  and  $\omega_1$ , where  $\omega_0 < \omega_1$  for the up-chirp, and vice versa for the down-chirp; the range of interest goes from  $0.8\omega_5$  to  $2.3\omega_5$ . A very long  $T$  is chosen to ensure a smooth and slow sweeping of the instantaneous frequency.

It is important to highlight that the chirp signal is applied on the free surface elevation; then, the wave-structure interaction applies a frequency-dependent amplitude modulation and phase shift for the two hydrodynamic DoFs. In the simplified case of linear hydrodynamics, the excitation force is constructed via the wave-to-force transfer functions, shown in Fig. 9, dependent on the wave frequency. In the more realistic case of NLFK model, there is also an implicit dependence on the wave height and on the displacement of the floater with respect to the free surface elevation.

Results of the up- and down-chirp simulations are shown in Fig. 7, with the colour gradient proportional to the wave height, ranging from almost zero (linear condition) to 4 m. The time traces are plotted against the instantaneous frequency, normalized by the pitching natural frequency  $\omega_5$ , since the frequency content linearly increases (or decreases) with time. Due to the period-doubling and nonlinear behaviour, the definition of the amplitude of response is not univocal; therefore, Fig. 7 shows the amplitude ( $\hat{z}$ ,  $\hat{\theta}$ , or  $\hat{\varepsilon}$ ) defined as the magnitude of the excursion between two consecutive extrema, i.e. the distance between a maximum ( $z_M$ ,  $\theta_M$ , or  $\varepsilon_M$ ) and the following minimum ( $z_m$ ,  $\theta_m$ , or  $\varepsilon_m$ ), which are also shown in Fig. 7.

Within the area close to the pitching natural period ( $\omega/\omega_5 = 1$ ), the pitch (and pendulum oscillation) response show a typical linear and symmetrical peak at very low wave amplitude, which is consistent with

the linear response assumption. As the wave height (and nonlinearity) increases, the response curve bends towards lower frequencies; in addition, the deformation of the curve becomes evident for higher wave heights, with an abrupt increase at low frequency and a smoother region afterwards. The same trend can be appreciated for the amplitude, maxima and minima.

Conversely, the trend in the heaving response is remarkably different, clearly showing a bifurcation as the effect of period doubling within the area close to the pitching natural period ( $\omega/\omega_5 = 1$ ). The top-right plot in Fig. 7 shows that the amplitude alternates between a high and a low value within two consecutive extrema; the difference between these two amplitudes is greater at the edges of the instability region, where the smaller amplitude is close to zero. A similar trend is found for the maxima and minima, which also alternate between two consecutive values; it is worth highlighting that, while the local maxima are almost always positive, the local minima present a branch that goes to well beyond positive values (bottom plots in Fig. 7 show minima with switched signs).

Finally, note that the crossing point between the two alternating branches of the amplitude, i.e. two consecutive equal  $\hat{z}$ , may wrongly induce thinking that the period-doubling response may have locally degenerated to a single-harmonic-looking response. However, this is incorrect, since the crossing points of the branches of the maxima and minima trends are at different frequency locations.

Considering all DoFs within the area close to the pitching natural period, only one curve can be distinguished: therefore, the two directions of the frequency sweep of the chirp signals are insignificant. Conversely, hysteresis phenomena are evident closer to the 2:1 parametric resonance region since, for each colour ( $H_w$ ), two lines can clearly be appreciated in all DoFs. The width of the parametric resonance region increases with the wave height, but the edge at higher frequency barely moves compared to the limit of instability at lower frequency. In addition, while a smooth amplitude transition can be remarked at higher frequency, an abrupt jump is obtained at the lower frequency boundary, due to a fold-type bifurcation. In fact, an unstable branch can be expected in between the two coexisting stable branches.

A clearer analysis of the hysteresis phenomenon resulting from the comparison of the up- and down-chirp response is performed in Fig. 8, where only one wave amplitude is shown. While the 1:1 region presents a perfect overlap between the two responses, a significant difference in the width of the 2:1 parametric resonance region can be appreciated, caused by a fold-type bifurcation. In particular, while the stemming point of the upper branch remains at the same higher frequency for both sweeping directions, the abrupt jump of the down-chirp response appears at a much smaller frequency than for the up-chirp, making the overall instability region larger.

The presence of coexisting attractors is a typical phenomenon of parametric resonance systems [19], which cannot be appreciated from a single-frequency analysis as in Fig. 4; conversely, the chirp analysis is able to reveal the actual and broader region of instability, which can be stimulated by panchromatic sea waves and leveraged by appropriate nonlinear control strategies.

## 7. Conclusion

This paper elaborates on the role of parametric resonance in wave energy converters: although parametric resonance is typically viewed as harmful and undesirable, if properly incorporated into the fundamental working principle and in the early design stages, it may actually increase the conversion bandwidth and efficiency. Based on these factors, a WEC with a 2:1 parametric resonance is suggested here, where one degree of freedom's natural period is purposefully double that of another degree of freedom, in order to use nonlinear hydrodynamic coupling to direct some of the external energy towards the power harvesting system.

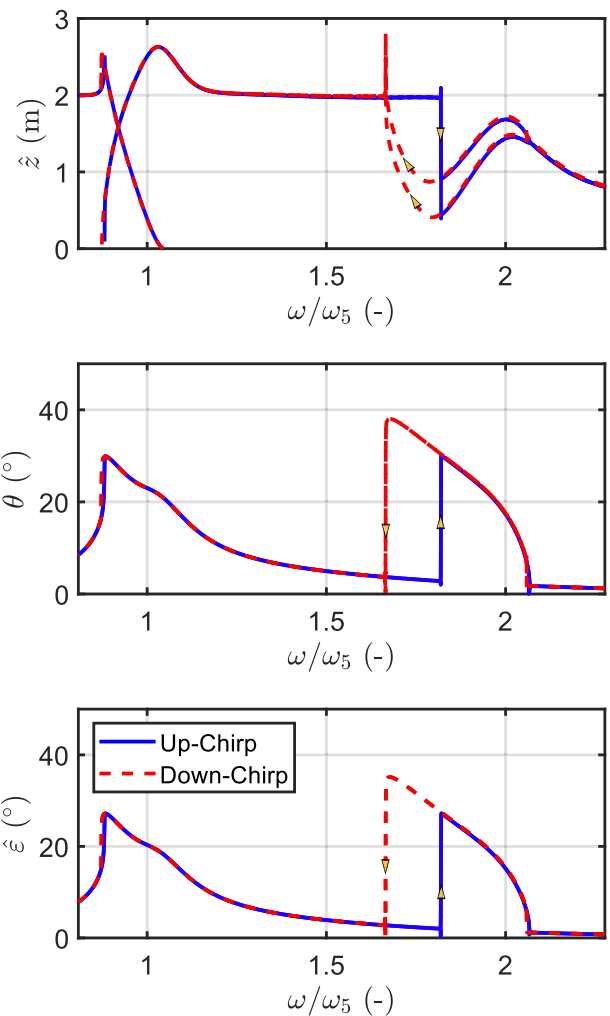


Fig. 8. Hysteresis phenomenon in the amplitude of the response: coexisting attractors resulting from up- and down-chirp input signals.

Exploiting this potential requires to appropriately address challenges in the mathematical modelling and energy-maximization control. Early design must be guided by computationally efficient mathematical models; only models that take into account a time-varying wetted surface can articulate parametric resonance. Therefore, for axisymmetric and prismatic floaters, this paper makes use of a computationally efficient formulation of nonlinear Froude–Krylov forces.

Thanks to the 2:1 parametric resonance condition herein proposed and to the appropriate numerical model, this paper quantitatively confirms that indeed parametric resonance does appear at the predicted conditions, and its magnitude is also meaningful: evidences are brought that the free response of the system shows amplitudes comparable to the natural frequency resonance, which entail a consequent significant increase in the available mechanical energy at the power take-off.

In addition, tools for analysing the nonlinear behaviour of the device are presented and results discussed; of particular practical interest is the effect of period doubling, which may have consequences on design and definition of physical constraints. Moreover, the presence of coexisting attractors makes the evaluation of hysteresis and the dimensions of the actual frequency bandwidth more delicate to the simulating tools.

In conclusion, this paper provides proofs that the free response has been indeed improved. This is the validation of a first notional step: parametric resonance has only provided a more fertile baseline

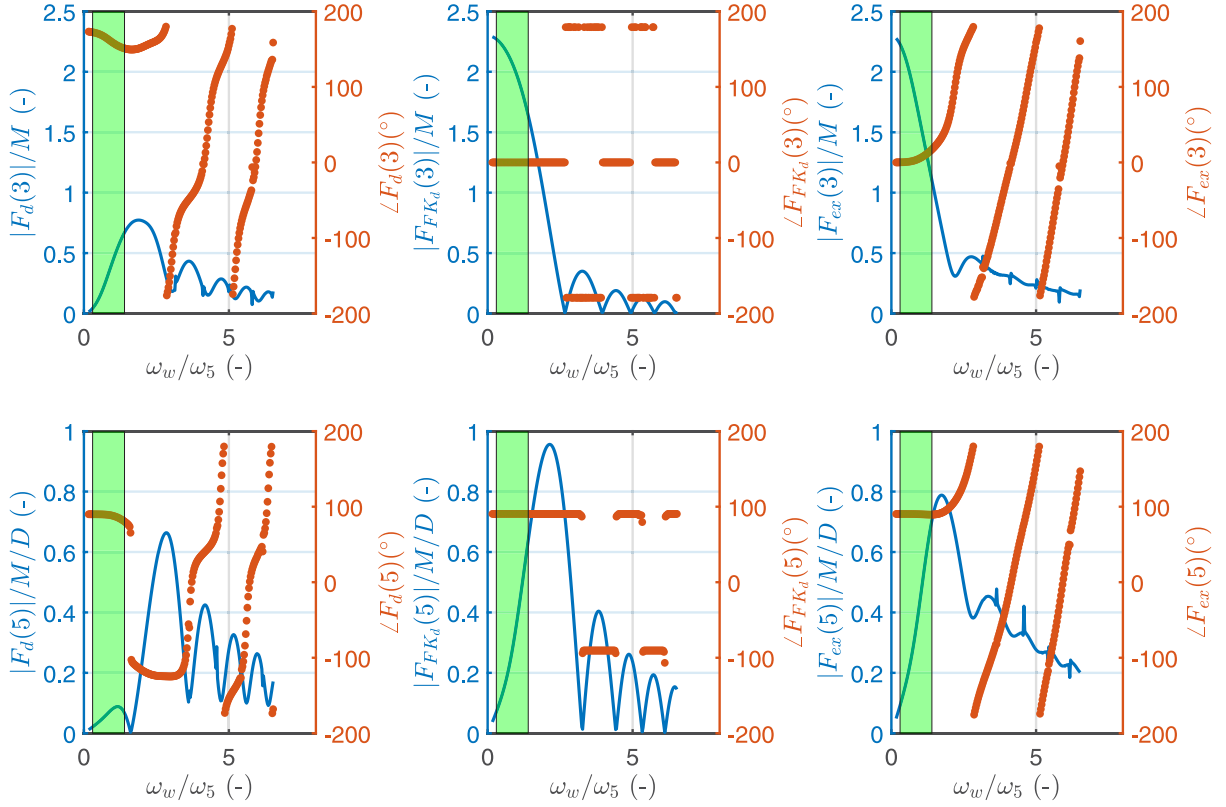


Fig. 9. From left to right: non-dimensional diffraction ( $F_d$ ), dynamic Froude-Krylov ( $F_{FK_d}$ ), and resulting excitation ( $F_{ex}$ ) linear hydrodynamic forces, in magnitude and phase, for heave (top row) and pitch (bottom row) degrees of freedom, for different incoming wave circular frequency ( $\omega_w$ ). The anonymization is performed by the mass ( $M$ ), draft ( $D$ ), and pitching natural frequency ( $\omega_5$ ). The green shaded area refers to the normalized frequency range of the incoming waves considered in the simulations.

with higher available energy; it is the role of an appropriate nonlinear control to actually exploit this potential for a final higher power output.

#### CRediT authorship contribution statement

**Giuseppe Giorgi:** Conceptualization, Data curation, Formal analysis, Funding acquisition, Investigation, Methodology, Project administration, Resources, Software, Supervision, Validation, Visualization, Writing – original draft, Writing – review & editing.

#### Declaration of competing interest

The authors declare that they have no known competing financial interests or personal relationships that could have appeared to influence the work reported in this paper.

#### Acknowledgements

Project funded under the National Recovery and Resilience Plan (NRRP), Italy, Mission 4 Component 2 Investment 1.3 - Call for tender No. 1561 of 11.10.2022 of Ministero dell'Università e della Ricerca (MUR); funded by the European Union – NextGenerationEU Award Number: Project code PE0000021, Concession Decree No. 1561 of 11.10.2022 adopted by Ministero dell'Università e della Ricerca (MUR), Italy, CUP, Italy E13C22001890001, Project title “Network 4 Energy Sustainable Transition – NEST”.

#### Appendix A. Hydrodynamic parameters

Figs. 9 and 10 show the linear hydrodynamic parameters of the hull herein considered. Eqs. (10) and (11) the state-space approximation of

convolution related to the radiation coefficients for heave and pitch DoFs, respectively.

$$\mathbf{A}_z^{ss} = \begin{bmatrix} -0.13821 & 1.1533 & -0.13821 & 0.13821 \\ -0.21243 & -0.80268 & 0.80268 & -0.80268 \\ -0.68874 & 0.68874 & -0.68874 & 2.5387 \\ -0.035803 & 0.035803 & -1.8858 & 0.035803 \end{bmatrix} \quad (10a)$$

$$\mathbf{B}_z^{ss} = [0.13821 \quad -0.80268 \quad 0.68874 \quad 0.035803]^T \quad (10b)$$

$$\mathbf{C}_z^{ss} = [5.0295 \cdot 10^5 \quad -7.8767 \cdot 10^5 \quad 4.8602 \cdot 10^4 \quad -8.2958 \cdot 10^5] \quad (10c)$$

$$\mathbf{A}_\theta^{ss} = \begin{bmatrix} 0.72678 & 0.65264 & 0.72678 & -0.72678 \\ -7.2388 & 5.8593 & -5.8593 & 5.8593 \\ -17.172 & 17.172 & -17.172 & 17.488 \\ -8.5847 & 8.5847 & -8.9015 & 8.5847 \end{bmatrix} \quad (11a)$$

$$\mathbf{B}_\theta^{ss} = [-0.72678 \quad 5.8593 \quad 17.172 \quad 8.5847]^T \quad (11b)$$

$$\mathbf{C}_\theta^{ss} = [1.8476 \cdot 10^7 \quad -1.8128 \cdot 10^7 \quad 2.3944 \cdot 10^6 \quad 2.3486 \cdot 10^6] \quad (11c)$$

#### Appendix B. Augmented time domain mathematical model

The augmented state vector includes the hydrodynamic DoFs ( $\xi_2$ ), the auxiliary vectors for the convolution integral ( $k_z$  and  $k_\theta$ ), and the pendulum oscillation ( $\varepsilon$ ) as follows:

$$\xi_{aug} = [z, \theta, \dot{z}, \dot{\theta}, k_z, k_\theta, \varepsilon, \dot{\varepsilon}]^T \quad (12)$$

Being the dimension of both  $k_z$  and  $k_\theta$  equal to 4, as shown in (10) and (11), the total size ( $\tilde{N}$ ) of  $\xi_{aug}$  is 14.



- [19] G. Habib, G. Giorgi, J. Davidson, Coexisting attractors in floating body dynamics undergoing parametric resonance, *Acta Mech.* 233 (2022) 2351–2367, <http://dx.doi.org/10.1007/S00707-022-03225-3>.
- [20] T.I. Fossen, H. Nijmeijer, *Parametric Resonance in Dynamical Systems*, Springer, 2012, <http://dx.doi.org/10.1007/978-1-4614-1043-0>.
- [21] N. Umeda, H. Hashimoto, S. Minegaki, A. Matsuda, N. Umeda, H. Hashimoto, S. Minegaki, A. Matsuda, An investigation of different methods for the prevention of parametric rolling, *J. Mar. Sci. Technol.* 13 (2008) 16–23, <http://dx.doi.org/10.1007/s00773-007-0253-x>.
- [22] H.K. Jang, M.H. Kim, Mathieu instability of Arctic Spar by nonlinear time-domain simulations, *Ocean Eng.* 176 (2019) 31–45, <http://dx.doi.org/10.1016/J.OCEANENG.2019.02.029>.
- [23] R. Gomes, J. Henriques, L. Gato, A. Falcă, Time-domain simulation of a slack-moored floating oscillating water column and validation with physical model tests, *Renew. Energy* 149 (2020) 165–180, <http://dx.doi.org/10.1016/J.RENENE.2019.11.159>.
- [24] G.S. Payne, J.R. Taylor, T. Bruce, P. Parkin, Assessment of boundary-element method for modelling a free-floating sloped wave energy device, Part 2: Experimental validation, *Ocean Eng.* 35 (2008) 342–357, <http://dx.doi.org/10.1016/J.OCEANENG.2007.10.008>.
- [25] J. Cordonnier, F. Gorintin, A. De Cagny, A.H. Clément, A. Babarit, SEAREV: Case study of the development of a wave energy converter, *Renew. Energy* 80 (2015) 40–52, <http://dx.doi.org/10.1016/J.RENENE.2015.01.061>.
- [26] A. Kurniawan, M. Grassow, F. Ferri, Numerical modelling and wave tank testing of a self-reacting two-body wave energy device, *Ships Offshore Struct.* 14 (2019) 344–356, <http://dx.doi.org/10.1080/17445302.2019.1595924>.
- [27] J. Orszaghova, H. Wolgamot, S. Draper, R. Eatock Taylor, P.H. Taylor, A. Rafiee, Transverse motion instability of a submerged moored buoy, *Proc. R. Soc. A: Math. Phys. Eng. Sci.* 475 (2019) <http://dx.doi.org/10.1098/rspa.2018.0459>.
- [28] J. Davidson, T. Kalmár-Nagy, A real-time detection system for the onset of parametric resonance in wave energy converters, *J. Mar. Sci. Eng.* 8 (819) (2020) <http://dx.doi.org/10.3390/jmse8100819>.
- [29] T.W. Ma, H. Zhang, N.S. Xu, A novel parametrically excited non-linear energy harvester, *Mech. Syst. Signal Process.* 28 (2012) 323–332, <http://dx.doi.org/10.1016/J.YMSSP.2012.01.017>.
- [30] X. Nie, S. Pei, T. Tan, Z. Yan, Z. Yan, Nonlinear 1:2 internal resonance response of L-shaped piezoelectric energy harvester under the influence of electrical damping, *Int. J. Mech. Sci.* 225 (2022) 107365, <http://dx.doi.org/10.1016/J.IJMECSCI.2022.107365>.
- [31] G. Giorgi, N. Faedo, Performance enhancement of a vibration energy harvester via harmonic time-varying damping: A pseudospectral-based approach, *Mech. Syst. Signal Process.* 165 (2022) 108331, <http://dx.doi.org/10.1016/J.YMSSP.2021.108331>.
- [32] D. Liu, Y. Wu, Y. Xu, J. Li, Stochastic response of bistable vibration energy harvesting system subject to filtered Gaussian white noise, *Mech. Syst. Signal Process.* 130 (2019) 201–212, <http://dx.doi.org/10.1016/j.ymssp.2019.05.004>.
- [33] S. Lenzi, M. Brocchini, C. Lorenzoni, Experimental rotations of a pendulum on water waves, *J. Comput. Nonlinear Dyn.* 7 (2012) <http://dx.doi.org/10.1115/1.4004547>.
- [34] D. Yurchenko, P. Alevras, Parametric pendulum based wave energy converter, *Mech. Syst. Signal Process.* 99 (2018) 504–515, <http://dx.doi.org/10.1016/j.ymssp.2017.06.026>.
- [35] V. Vaziri, A. Najdecka, M. Wiercigroch, Experimental control for initiating and maintaining rotation of parametric pendulum, *Eur. Phys. J. Special Top.* 223 (4) (2014) 795–812, <http://dx.doi.org/10.1140/EPJST/E2014-02141-Y>.
- [36] F. Reguera, F.E. Dotti, S.P. Machado, Rotation control of a parametrically excited pendulum by adjusting its length, *Mech. Res. Commun.* 72 (2016) 74–80, <http://dx.doi.org/10.1016/J.MECHRESCOM.2016.01.011>.
- [37] S. Zou, O. Abdelkhalik, R. Robinett, U. Korde, G. Bacelli, D. Wilson, R. Coe, Model Predictive Control of parametric excited pitch-surge modes in wave energy converters, *Int. J. Mar. Energy* 19 (2017) 32–46, <http://dx.doi.org/10.1016/J.IJOME.2017.05.002>.
- [38] B. Orazov, O.M. O'Reilly, S. Savaş, On the dynamics of a novel ocean wave energy converter, *J. Sound Vib.* 329 (2010) 5058–5069, <http://dx.doi.org/10.1016/J.JSV.2010.07.007>.
- [39] H. Zhang, X. Zhou, D. Xu, W. Zou, J. Ding, S. Xia, Nonlinear stiffness mechanism for high-efficiency and broadband raft-type wave energy converters, *Mech. Syst. Signal Process.* 177 (2022) 109168, <http://dx.doi.org/10.1016/j.ymssp.2022.109168>.
- [40] M.A. Khasawneh, M.F. Daqaq, Experimental assessment of the performance of a bi-stable point wave energy absorber under harmonic incident waves, *Ocean Eng.* 280 (2023) 114494, <http://dx.doi.org/10.1016/J.OCEANENG.2023.114494>.
- [41] F. Carapellese, E. Pasta, S.A. Sirigu, N. Faedo, SWINGO: Conceptualisation, modelling, and control of a swinging omnidirectional wave energy converter, *Mech. Syst. Signal Process.* 197 (2023) 110356, <http://dx.doi.org/10.1016/J.YMSSP.2023.110356>.
- [42] E. Al Shami, X. Wang, X. Ji, A study of the effects of increasing the degrees of freedom of a point-absorber wave energy converter on its harvesting performance, *Mech. Syst. Signal Process.* 133 (2019) <http://dx.doi.org/10.1016/j.ymssp.2019.106281>.
- [43] F. Carapellese, E. Pasta, B. Paduano, N. Faedo, G. Mattiazzo, Intuitive LTI energy-maximising control for multi-degree of freedom wave energy converters: The PeWEC case, *Ocean Eng.* 256 (2022) 111444, <http://dx.doi.org/10.1016/J.OCEANENG.2022.111444>.
- [44] D.G. Gioia, E. Pasta, P. Brandimarte, G. Mattiazzo, Data-driven control of a pendulum wave energy converter: A Gaussian process regression approach, *Ocean Eng.* 253 (2022) 111191, <http://dx.doi.org/10.1016/J.OCEANENG.2022.111191>.
- [45] B. Battisti, G. Giorgi, G.V. Fernandez, Balancing power production and coastal protection: A bi-objective analysis of Wave Energy Converters, *Renew. Energy* 220 (2024) 119702, <http://dx.doi.org/10.1016/J.RENENE.2023.119702>.
- [46] J. Liu, A. Meucci, Q. Liu, A.V. Babanin, D. Ierodiaconou, X. Xu, I.R. Young, A high-resolution wave energy assessment of south-east australia based on a 40-year hindcast, *Renew. Energy* 215 (2023) 118943, <http://dx.doi.org/10.1016/J.RENENE.2023.118943>.
- [47] M. Penalba, C. Guo, A. Zarketa-Astigarraga, G. Cervelli, G. Giorgi, B. Robertson, Bias correction techniques for uncertainty reduction of long-term meteocean data for ocean renewable energy systems, *Renew. Energy* 219 (2023) 119404, <http://dx.doi.org/10.1016/J.RENENE.2023.119404>.
- [48] G. Cervelli, L. Parrinello, C. Moscoloni, G. Giorgi, Comparison of the ERA5 wave forecasting dataset against buoy record, *Instrum. Mesure Métrol.* 21 (2022) 87–95, <http://dx.doi.org/10.18280/im.21.0301>.
- [49] A. Babarit, G. Delhommeau, Theoretical and numerical aspects of the open source BEM solver NEMOH, in: *Proceedings of the 11th European Wave and Tidal Energy Conference, 2015*, pp. 1–12, hal-01198800.
- [50] I. Wamit, WAMIT User Manual, 2019, <http://dx.doi.org/10.1017/CBO9781107415324.004>.
- [51] G. Giorgi, J.V. Ringwood, Comparing nonlinear hydrodynamic forces in heaving point absorbers and oscillating wave surge converters, *J. Ocean Eng. Mar. Energy* 4 (2018a) 25–35, <http://dx.doi.org/10.1007/s40722-017-0098-2>.
- [52] T. Perez, T.I. Fossen, Practical aspects of frequency-domain identification of dynamic models of marine structures from hydrodynamic data, *Ocean Eng.* (2010).
- [53] N. Faedo, Y. Peñ-Sánchez, J.V. Ringwood, Finite-Order Hydrodynamic Model Determination for Wave Energy Applications Using Moment-Matching, *Ocean Eng.* 163 (2018) 251–263.
- [54] N. Pozzi, G. Bracco, B. Passione, S.A. Sirigu, G. Mattiazzo, PeWEC: Experimental validation of wave to PTO numerical model, *Ocean Eng.* 167 (2018) 114–129, <http://dx.doi.org/10.1016/J.OCEANENG.2018.08.028>.
- [55] G. Giorgi, J.V. Ringwood, Relevance of pressure field accuracy for nonlinear Froude–Krylov force calculations for wave energy devices, *J. Ocean Eng. Mar. Energy* 4 (2018b) 57–71, <http://dx.doi.org/10.1007/s40722-017-0107-5>.
- [56] G. Giorgi, Nonlinear Froude–Krylov Matlab demonstration toolbox, 2019, <http://dx.doi.org/10.5281/zenodo.4682671>.
- [57] M. Folley, *Numerical Modelling of Wave Energy Converters - State of the Art Techniques for Single Devices and Arrays*, Elsevier, 2016.
- [58] N. Faedo, G. Giorgi, J.V. Ringwood, G. Mattiazzo, Optimal control of wave energy systems considering nonlinear Froude–Krylov effects: control-oriented modelling and moment-based control, *Nonlinear Dynam.* 109 (2022b) 1777–1804, <http://dx.doi.org/10.1007/s11071-022-07530-3>.